

Article

Hydrothermal Pre-Carbonization Triggers Structural Reforming Enabling Pore-Tunable Hierarchical Porous Carbon for High-Performance Supercapacitors

Cuihua Kang ^{1,2}, Mingyuan Zuo ³, Chang Qiu ⁴, Fanda Zeng ¹, Yuehui Wang ¹, Zhuo Chen ¹, Tingting Liang ¹ and Daping Qiu ^{1,3,*}

¹ Hubei Provincial Collaborative Innovation Center for New Energy Microgrid, College of Electrical Engineering & New Energy, China Three Gorges University, Yichang 443002, China

² Analysis and Testing Center, China Three Gorges University, Yichang 443002, China

³ State Key Laboratory of Chemical Resource Engineering, Beijing Key Laboratory of Electrochemical Process and Technology for Materials, Beijing University of Chemical Technology, Beijing 100029, China

⁴ China Construction Third Engineering Bureau Group Co., Ltd., Wuhan 430064, China

* Correspondence: qiudaping@ctgu.edu.cn

Abstract: The engineering of pore structures has great significance in the development of high-performance carbon-based supercapacitor electrode materials. Herein, we have successfully transformed jujube pits into hierarchical porous carbon (HJPC-4) with excellent capacitive properties via a unique hydrothermal–carbonization–activation strategy. Hydrothermal pretreatment is essential to regulate the supermesoporous and macroporous structure of samples and their superior electrochemical performances. Owing to the large ion-accessible, remarkable supermesoporous and macroporous pore volume, HJPC-4 exhibited ultra-high specific capacitance (6 M KOH: 316 F g^{-1} at 1 A g^{-1} ; EMIMBF₄: 204 F g^{-1} at 1 A g^{-1}), excellent rate performance (6 M KOH: 231 F g^{-1} at 100 A g^{-1} ; EMIMBF₄: 154 F g^{-1} at 30 A g^{-1}), outstanding cycling stability (6 M KOH: the retention rate is 92.11% after 60,000 cycles at 10 A g^{-1} ; EMIMBF₄: the retention rate is 80% after 10,000 cycles at 5 A g^{-1}), and ultimate energy/power density up to $91.09 \text{ Wh kg}^{-1}/24.25 \text{ kW kg}^{-1}$ in EMIMBF₄ two-electrode systems. This work presents unique insights into the effect of the pore structure of carbon-based materials on their capacitive energy storage.



Academic Editor: Ottorino Veneri

Received: 28 November 2024

Revised: 24 December 2024

Accepted: 24 December 2024

Published: 26 December 2024

Citation: Kang, C.; Zuo, M.; Qiu, C.;

Zeng, F.; Wang, Y.; Chen, Z.; Liang, T.; Qiu, D. Hydrothermal

Pre-Carbonization Triggers Structural Reforming Enabling Pore-Tunable Hierarchical Porous Carbon for High-Performance Supercapacitors.

Batteries **2025**, *11*, 7. <https://doi.org/10.3390/batteries11010007>

Copyright: © 2024 by the authors. Licensee MDPI, Basel, Switzerland. This article is an open access article distributed under the terms and conditions of the Creative Commons Attribution (CC BY) license (<https://creativecommons.org/licenses/by/4.0/>).

1. Introduction

Supercapacitors (SCs), as the new generation of efficient energy storage devices, have garnered increasing attention due to their long cycle life, excellent safety, and fast-charging capability over a wide temperature range [1–3]. Unfortunately, the low energy density of SCs limits their large-scale applications in electric vehicles, portable electronic devices, and power storage [4–6]. Electrode materials, being the core component of SCs, have a deterministic effect on their electrochemical performance. In comparison with electrode materials such as metal oxides [7], conducting polymers [8], carbon nanotubes [9], graphene [10,11], carbon fibers [12], etc., the conversion of low-cost, resource-rich, environmentally friendly and renewable biomass waste into porous carbon electrode materials can not only alleviate the increasingly severe energy crisis but also make a great contribution to environmental protection [13]. Studies have shown that hierarchical porous carbon is the ideal electrode material for high-performance SCs [14]. Nonetheless, due to the undefined components

and complex structure of most biomass, the pore structure of biomass-derived carbon is difficult to regulate, which leads to the poor electrochemical properties of biomass-derived carbon [15–17]. Consequently, the pore structure regulation engineering of biomass-derived carbon is significant for the development of high-performance hierarchical porous carbon electrode materials.

In light of the energy storage processes dominated by electrochemical double-layer capacitance (EDLC), the hierarchical pore structure plays a crucial role in the capacitive energy storage process of carbon-based materials [18,19]. As is well known, ion-accessible micropores and small-sized mesopores are the main contributors to the high specific surface area of carbon materials. They provide a high-affinity electrode/electrolyte interface and abundant active sites for ion adsorption/desorption to enhance EDLC. In addition, supermesopores offer fast channels for electrolyte permeation and ion transfer to improve rate performance, and macropores act as “buffers” to store more electrolytes [18,20]. Owing to the complex microstructure of biomass and the strong interaction between biomass components, it is challenging to tailor the pore structure of porous carbon through conventional carbonization–activation processes. The template method (hard template: silica, zeolite, zinc oxide; soft template: F127, P123) is an effective method to prepare hierarchical porous carbon with a tunable pore structure [21,22]. However, the template method usually involves harsh experimental conditions, is time consuming, and is expensive, which greatly limits its large-scale application [23]. Therefore, it remains a great challenge to control the structure of porous carbon and balance the ratio of different pore sizes while satisfying simplicity, low cost, and sustainability. In recent years, lignocellulosic-based biomass materials (composed of cellulose, hemicellulose, and lignin) such as wood [24], bagasse [25,26], coconut shells [27], and wheat straw [28] have been widely transformed into porous carbon electrodes for SCs. It is worth noting that some of the unstable components, such as hemicellulose and cellulose, in biomass precursors can be removed by hydrothermal treatment to form interconnected nanopores. Subsequently, combined with molten salt activation, it can further increase the percentage of micropores and mesopores [26]. In addition, doping porous carbon with heteroatoms can improve the electrical conductivity and surface wettability of carbon materials as well as provide additional pseudocapacitance [29–31].

The energy density of SCs is positively correlated with the specific capacity of the device and the square of the operating voltage. Hence, the construction of high energy density SCs requires electrolytes with a wide electrochemical stability potential window in addition to electrode materials with high capacity [32]. Due to the limited voltage of water decomposition (1.23 V), the operating voltage of aqueous electrolyte-based supercapacitors is generally within 1.3 V [33]. Although organic electrolytes have a wider electrochemical window (2.5–2.8 V), they have disadvantages such as flammability, toxicity, and volatility. In contrast, ionic liquids with excellent chemical stability, nonflammability, and a wide electrochemical window (~4 V) show great advantages in fabricating high energy density SCs [34].

As is well known, jujube pits are typical lignocellulosic-based biomass materials. In this work, using jujube pits as the precursor, we proposed a hydrothermal–carbonization–activation strategy to synthesize hierarchical porous carbon (HJPC) with ultra-high specific surface area, reasonable pore size distribution and oxygen-functional group content. Among them, a phosphoric acid-assisted hydrothermal step can activate the carbon framework of the biomass precursor, and the carbonization–activation process plays a role in modulating the pore structure. Thanks to the unique structural features, the optimized HJPC-4-based supercapacitor exhibits excellent electrochemical performance in both 6 M KOH aqueous electrolyte and 1-ethyl-3-methylimidazolium tetrafluoroborate (EMIMBF₄) electrolyte. Excitingly, the optimal SCs in EMIMBF₄ electrolyte can provide an exception-

ally high energy density of 91.09 Wh kg^{-1} at a power density of 896 W kg^{-1} and still contribute a high energy density of 55.72 Wh kg^{-1} even at an ultra-high power density of 24.25 kW kg^{-1} .

2. Materials and Methods

2.1. Materials

Jujube pits were sourced from Xinjiang, China. Other analytical grade chemicals were purchased from Sinopharm Chemical Reagent Co., Ltd. (Shanghai, China), and all chemical reagents were used directly without purification.

2.2. Preparation of Hierarchical Porous Carbon

The jujube pits were washed, dried, and then pulverized into powder. Then, jujube pits powder (6 g) and 5 wt % phosphoric acid solution (60 mL) were added to an autoclave. The autoclave was heated in an oven at 180°C for 16 h and cooled naturally. The hydrothermal product (HJPs-180) was collected by filtrating and then dried at 80°C overnight. The dried HJPs-180 was carbonized at 600°C for 2 h under a nitrogen atmosphere in a tube furnace. The remaining residue was washed, filtered, and dried. Subsequently, 0.6 g of the residues and a certain amount of KOH was taken in deionized water and stirred for 2 h to form a homogeneous suspension, which was subsequently transferred to an oven for drying. The dried mixture was activated at 800°C for 2 h under a nitrogen atmosphere. The collected residue was washed several times with deionized water until neutral and then dried in an oven at 80°C for 24 h. The activation samples were named as HJPC-X ($X = 2, 3, 4$, and 5), where X represents the mass ratio of KOH to hydrothermal carbon. The preparation of JPC-4 was the same as that of HJPC-X except that it was not subjected to hydrothermal treatment.

2.3. Materials Characterization

The morphology and structure of the prepared samples were observed by scanning electron microscopy (TESCAN, MIRA LMS, Warrendale, PA, USA) and transmission electron microscopy (FEI, TECNAI G2 F20, Lausanne, Switzerland). The effect of hydrothermal treatment on the surface functional groups of jujube pits was examined by Fourier transform infrared spectroscopy (Thermo Fisher, Nicolet-6700, Waltham, MA, USA). X-ray diffractometer (Rigaku, Smartlab-SE, Auburn Hills, MI, USA) and Raman spectrometer (HORIBA, XploRA PLUS, Kyoto, Japan) were applied to determine the crystallographic features and structural defects of the samples. X-ray photoelectron spectroscopy (SHIMADZU, AXIS Supra, Kyoto, Japan) was used to test the elemental composition and chemical states of samples. The specific surface area and porosity of porous carbon materials were analyzed and calculated based on the Brunauer–Emmett–Teller (BET) model and DFT theory by means of an N_2 adsorption analyzer (Micromeritics, ASAP 2020, Norcross, GA, USA).

2.4. Electrochemical Measurements

The active material, acetylene black, and polytetrafluoroethylene (PTFE) were added to 10 mL ethanol with the ratio of 8:1:1 and ground evenly until a viscous slurry was formed, and then the slurry was rolled into a film with a roller press. The film was cut into 12 mm diameter discs and dried at 80°C in an oven. Subsequently, the dried electrode discs are placed on nickel foam and pressed into flat sheets as working electrodes with a press at 10 MPa. The mass loading of active materials was about $2.5\text{--}3 \text{ mg cm}^{-2}$. The electrochemical performances of HJPC-X and JPC-4 were evaluated in a CR2032 coin-cell with 6 M KOH or EMIMBF₄ electrolyte. Cyclic voltammetry (CV) and galvanostatic charge–discharge (GCD) were tested at the electrochemical workstation (CHI 760E) and

battery test system (LANHE, CT2001A). The specific capacitance and specific energy/power densities of the two-electrode system were defined in our previous work [18].

3. Results and Discussion

Figure 1a displays the preparation steps of HJPC-X, which mainly include hydrothermal treatment in diluted phosphoric acid solution followed by carbonization-KOH etching. The scanning electron microscopy (SEM) images in Figure 1b–d show that JPC-4 without hydrothermal treatment is composed of carbon blocks with relatively smooth surfaces, where the carbon blocks are distributed with pits about 1 μm in diameter. In contrast, the carbon blocks in hydrothermally treated HJPC-4 (Figure 1e,f) exhibit a porous and loose structure. Remarkably, the original blocks appear to have been refined into nanoparticles. Notably, the morphological characteristics of HJPC-2 (Figure S1a,b), HJPC-3 (Figure S1c,d), and HJPC-5 (Figure S1e,f) are similar to that of HJPC-4, which is sufficient to indicate that hydrothermal treatment has an obvious impact on the morphology of porous carbon. It is well known that jujube pits (JPs) are lignocellulosic-based biomass materials composed of cellulose, hemicellulose, lignin, and trace minerals [35]. In a hydrothermal scenario, phosphoric acid can catalyze the cellulose in JPs hydrolyze into oligosaccharides, inducing the formation of a multi-cavity framework. In short, HJPC-X displays a loose structure with abundant pores, which is favorable for the electrolyte to penetrate through the surface and reach the interior of the carbon material electrode, thus enhancing the electrochemical capacitive performance of the carbon material.

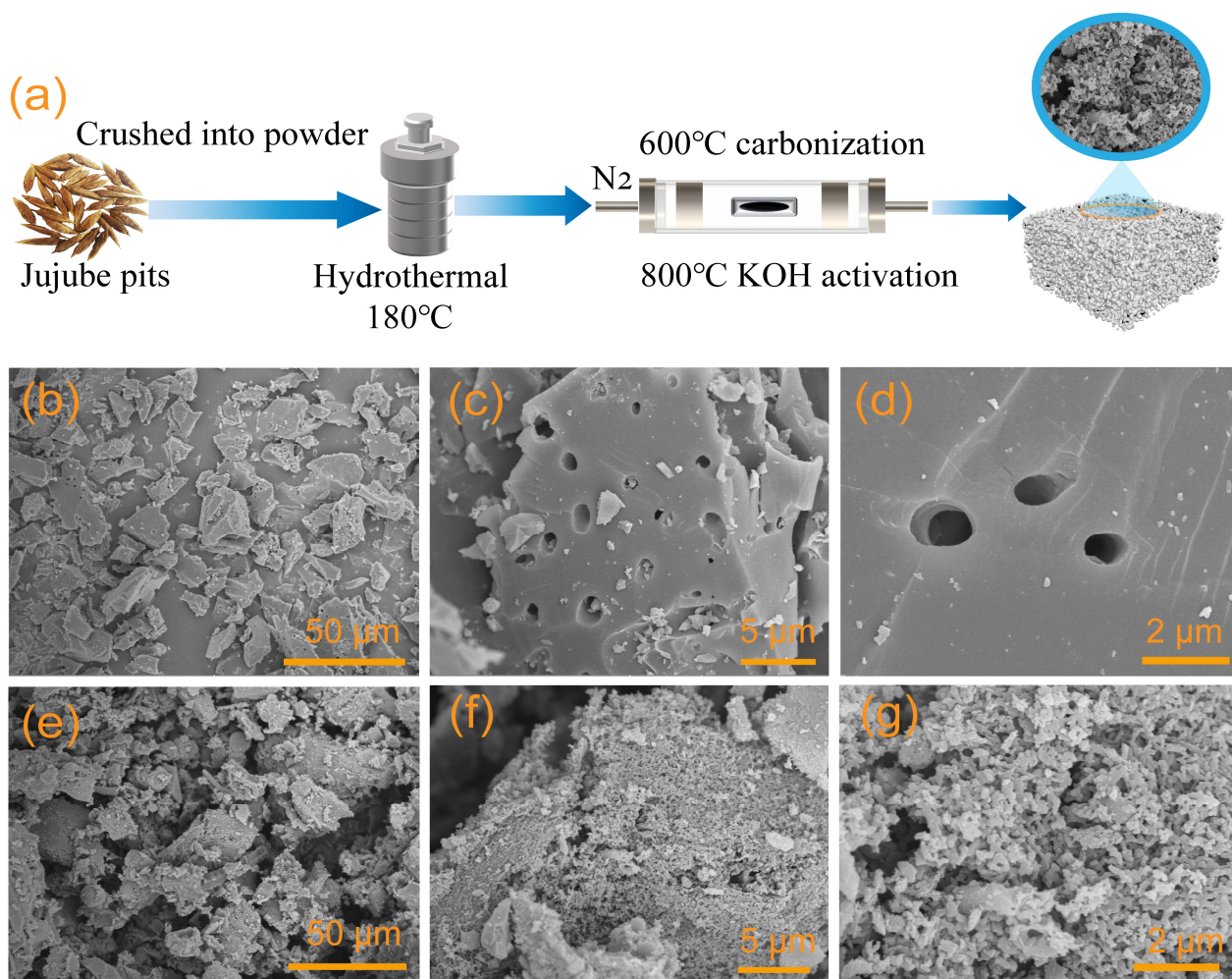


Figure 1. (a) Schematic diagrams of the synthetic route for HJPC-X. SEM images of (b–d) JPC-4; (e–g) HJPC-4.

Transmission electron microscopy (TEM) was employed to further analyze the nanostructure of the material. JPC-4 presents as dense carbon blocks (Figure 2a) presumably without the formation of obvious pores. The TEM image of HJPC-4 is shown in Figure 2c, demonstrating the morphology of nanosheets with abundant supermesopores and macropores distributed (blue line areas). Furthermore, the high-resolution TEM images in Figure 2b,d indicate that the severe etching of the carbon framework by KOH results in a highly amorphous structure of JPC-4 and HJPC-4. To investigate the elements distribution in HJPC-4, the HAADF-STEM was used (Figure 2e). As shown in Figure 2f–h, C and O are evenly distributed in the region.

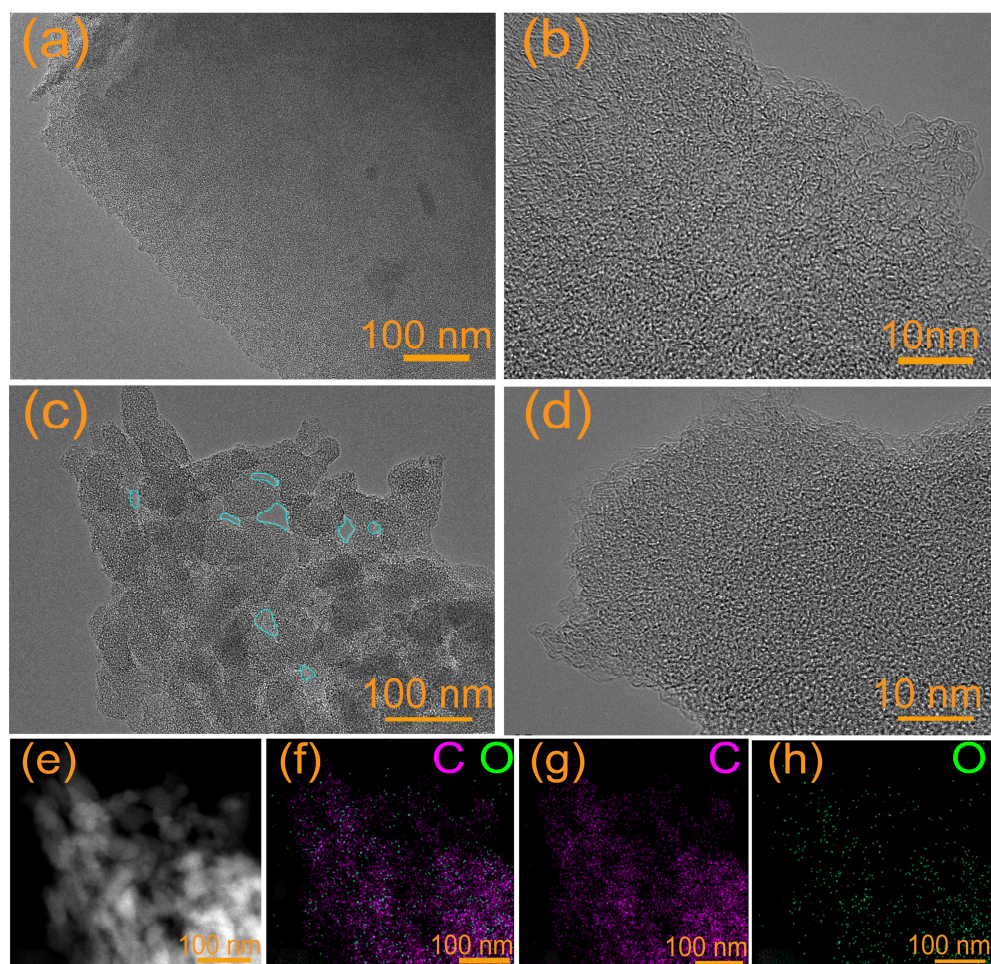


Figure 2. TEM images (a,b) of JPC-4, (c,d) HJPC-4. (e) High-angle annular dark-field-scanning transmission electron microscopy image of HJPC-4, (f–h) EDS elemental mapping of HJPC-4.

Fourier transform infrared (FTIR) was performed to investigate the impact of hydrothermal treatment on the functional groups of JPs. As shown in Figure 3a, the FTIR spectra of JPs exhibited features attributed to their main components (cellulose, hemicellulose, and lignin). Notably, the spectral bands at 1735 cm^{-1} (orange region) and $1200\text{--}1000\text{ cm}^{-1}$ (blue region) of the hydrothermally treated sample (HJPs-180) are largely diminished or even disappeared, which confirms that most of the hemicellulose and cellulose can be removed in the hydrothermal treatment. However, the spectral band representing the functional groups of lignin (pink region) did not change significantly after hydrothermal treatment, which indicates that the main composition of the hydrothermally treated samples is lignin.

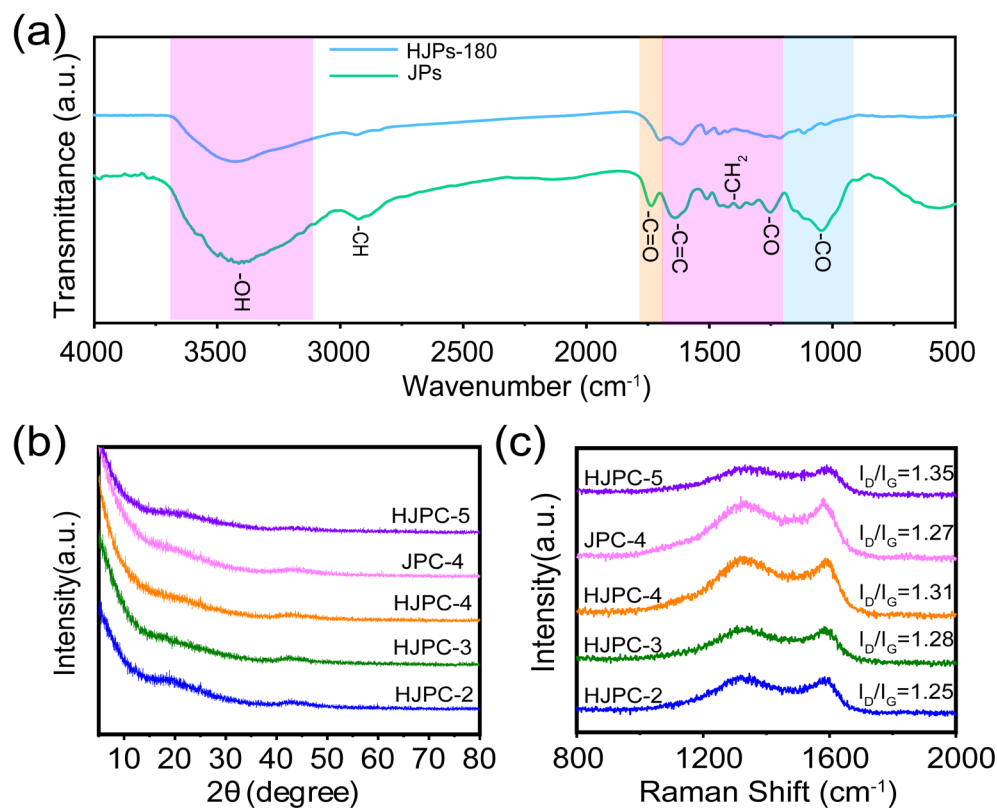


Figure 3. (a) FTIR spectra of JPs and HJPs-180. (b) XRD patterns, (c) Raman spectra of HJPC-X and JPC-4.

X-ray diffraction (XRD) and Raman spectroscopy were used to analyze the crystallographic characteristics of the samples. The two peaks at 20.1° and 43.5° of the XRD pattern represent the (002) and (100) planes of graphite, respectively, which indicate the highly amorphous structural features of the prepared samples (Figure 3b) [36,37]. Notably, the XRD diffraction peaks of the samples become wider and weaker with an increase in the KOH ratio, which is attributed to more defects produced by the intense etching of the carbon framework with excess KOH. As displayed in Figure 3c, the characteristic peaks of Raman spectra at 1360 and 1580 cm^{-1} indicate the D peak (disorder and defects) and G peak (ordered graphite structure), respectively. The HJPC-X and JPC-4 samples have high values of I_D/I_G up to 1.25 – 1.35 , further confirming their defect-rich crystallographic features [38]. In addition, the XRD pattern of HJPC-4 shows wider diffraction peaks and higher I_D/I_G values than JPC-4, which also indicates that the hydrothermal treatment introduced more defects and disordered structures.

N_2 adsorption–desorption test was applied to the analysis of the specific surface area (SSA) and porosity of the samples. Figure 4a shows the N_2 adsorption–desorption isotherms of HJPC-X and JPC-4. HJPC-X displays a sharp increase in N_2 adsorption at the low relative pressure ($0 < P/P_0 < 0.1$), indicating their micropores-dominated characteristics. Meanwhile, the isotherm is upward in the tail of the high-pressure part ($0.9 < P/P_0 < 1.0$), meaning that HJPC-X includes supermesopores ($d > 20\text{ nm}$) or macropores [39,40]. JPC-4 shows a typical type I isotherm, which suggests that it is a microporous material. The pore size of JPC-4 is concentrated below 2.5 nm , while HJPC-X presents a hierarchical porous structure with the coexistence of micropores, supermesopores, and macropores (Figure 4b). The detailed pore parameters of HJPC-X and JPC-4 are presented in Figure 4c and Table S1. HJPC-4 has a higher SSA ($2771.4\text{ m}^2\text{ g}^{-1}$ vs. $2594.5\text{ m}^2\text{ g}^{-1}$) and a larger pore volume ($1.495\text{ cm}^3\text{ g}^{-1}$ vs. $1.066\text{ cm}^3\text{ g}^{-1}$) compared to JPC-4, which is attributed to the hydrothermal treatment activating the supermesopores and macropores of JPs. However, with a

further increase in the dose of KOH, the pore volume of HJPC-5 decreased ($1.342 \text{ cm}^3 \text{ g}^{-1}$), which may be owing to the collapse of the pore structure caused by the excessive KOH dose. Notably, for the energy storage process in carbon-based supercapacitors, the reversible adsorption/desorption of active ions in the pores is only possible if the pore diameter is larger than the active ion solvation radius (ion accessible pores), and pores with too large sizes (such as $d > 3 \text{ nm}$) are not favorable for the contribution of active sites [41]. For KOH electrolytes, ions in aqueous solutions are almost inaccessible to micropores below 0.5 nm, and for EMIMBF₄ electrolytes (BF₄⁻ is 0.33 nm, EMIM⁺ is 0.76 nm), only pores above 0.76 nm can provide active sites [41,42]. Hence, we defined the 0.5–3 nm and 0.76–3 nm pores as reactive ion-accessible pores based on the 6 M KOH electrolyte and EMIMBF₄ electrolyte. As shown in Figure 4c and Table S1, HJPC-4 has not only the highest SSA ($2771.4 \text{ m}^2 \text{ g}^{-1}$) and pore volume ($1.495 \text{ cm}^3 \text{ g}^{-1}$) but also the highest pore volume suitable for the KOH solution ($1.067 \text{ cm}^3 \text{ g}^{-1}$) and the EMIMBF₄ ($1.025 \text{ cm}^3 \text{ g}^{-1}$). In addition, the hydrothermal strategy can activate the supermesopores and macropores of HJPC-X (HJPC-2: $0.445 \text{ cm}^3 \text{ g}^{-1}$; HJPC-3: $0.263 \text{ cm}^3 \text{ g}^{-1}$; HJPC-5: $0.27 \text{ cm}^3 \text{ g}^{-1}$) to provide channels for rapid ion transport, which contributes to their rate performance.

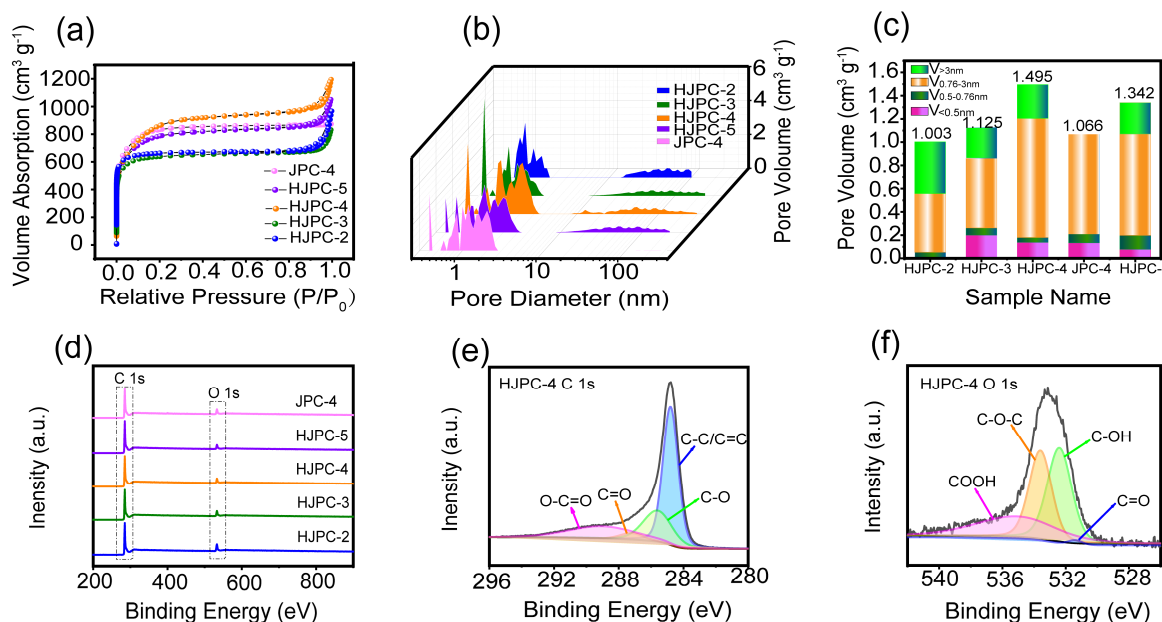


Figure 4. (a) N_2 adsorption–desorption isotherms, (b) pore size distribution, (c) pore volume histograms, (d) XPS survey spectra of HJPC-X and JPC-4. (e) High-resolution C1s spectra, (f) O 1s spectra of HJPC-4.

X-ray photoelectron spectroscopy (XPS) was used to conduct a more in-depth investigation of the element configurations of HJPC-X and JPC-4. As observed in Figure 4d and Table S2, two peaks in the survey spectra at approximately 286 and 534 eV are attributed to C and O [41,43], which indicates that O (9.52, 7.9, 6.53, 6.4, and 7.53% for HJPC-2, HJPC-3, HJPC-4, HJPC-5, and JPC-4, respectively) has been successfully doped into the carbon framework. The C 1s spectra can be deconvoluted into four peaks, including C-C/C=C (284.8 eV), C-O (285.6 eV), C=O (287.82 eV), and O-C=O (289 eV) (Figures 4e and S2a) [43]. Further, the deconvoluted O 1s spectra imply four kinds of O-containing species: quinone-O (531.4 eV), phenol-O (532.4 eV), ether-O (533.6 eV), and carboxyl-O (535.1 eV) (Figures 4f and S2b) [43]. It is widely acknowledged that O-containing functional groups can enhance the hydrophilicity of electrode materials and provide additional pseudocapacitance through the Faradaic reaction.

The electrochemical performance of HJPC-X and JPC-4 was first evaluated by assembling symmetrical supercapacitors in a 6 M KOH electrolyte. As shown in Figure 5a, the CV curves at 100 mV s^{-1} of all samples exhibit a nearly quasi-rectangular shape, indicating a perfect EDLC behavior. Furthermore, the largest integrated area of HJPC-4 reveals its highest specific capacitance. Consistent with the CV result, the longest discharge time of HJPC-4 in the GCD curves (Figure 5b) further corroborates the conclusion in CV analysis. The specific capacitances of HJPC-X and JPC-4 calculated based on the GCD curves (Figures S3 and 5e,f) are shown in Figure 5c. HJPC-4 displays an ultra-high specific capacitance of 316 F g^{-1} at 1 A g^{-1} , which is superior to other samples. Moreover, its specific capacitance is $312, 291, 277, 263, 259, 247$, and 231 F g^{-1} at $2, 5, 10, 20, 30, 50$, and 100 A g^{-1} , respectively, and the capacitance retention rate is as high as 73.1% at 100 A g^{-1} . Additionally, HJPC-2, HJPC-3, and HJPC-5 have ultra-high capacitance retention rates of 71.6%, 73%, and 75.3% even after 100-fold current density expansion. However, JPC-4 (189 F g^{-1} at 100 A g^{-1} with 65.9% capacitance retention) demonstrates a relatively poor specific capacitance and capacitance retention rate compared to HJPC-4. It indicates that the hydrothermal treatment plays an important role in the capacitive performance of the JPs-derived carbon. Moreover, as displayed in Figure 5d, the CV curve of HJPC-4 still maintains a nearly rectangular shape even at 600 mV s^{-1} , further confirming its excellent rate capability. In Figure 5e,f, the GCD curves of HJPC-4 at different current densities are all approximately isosceles triangles, once again proving the energy storage behavior dominated by EDLC [44].

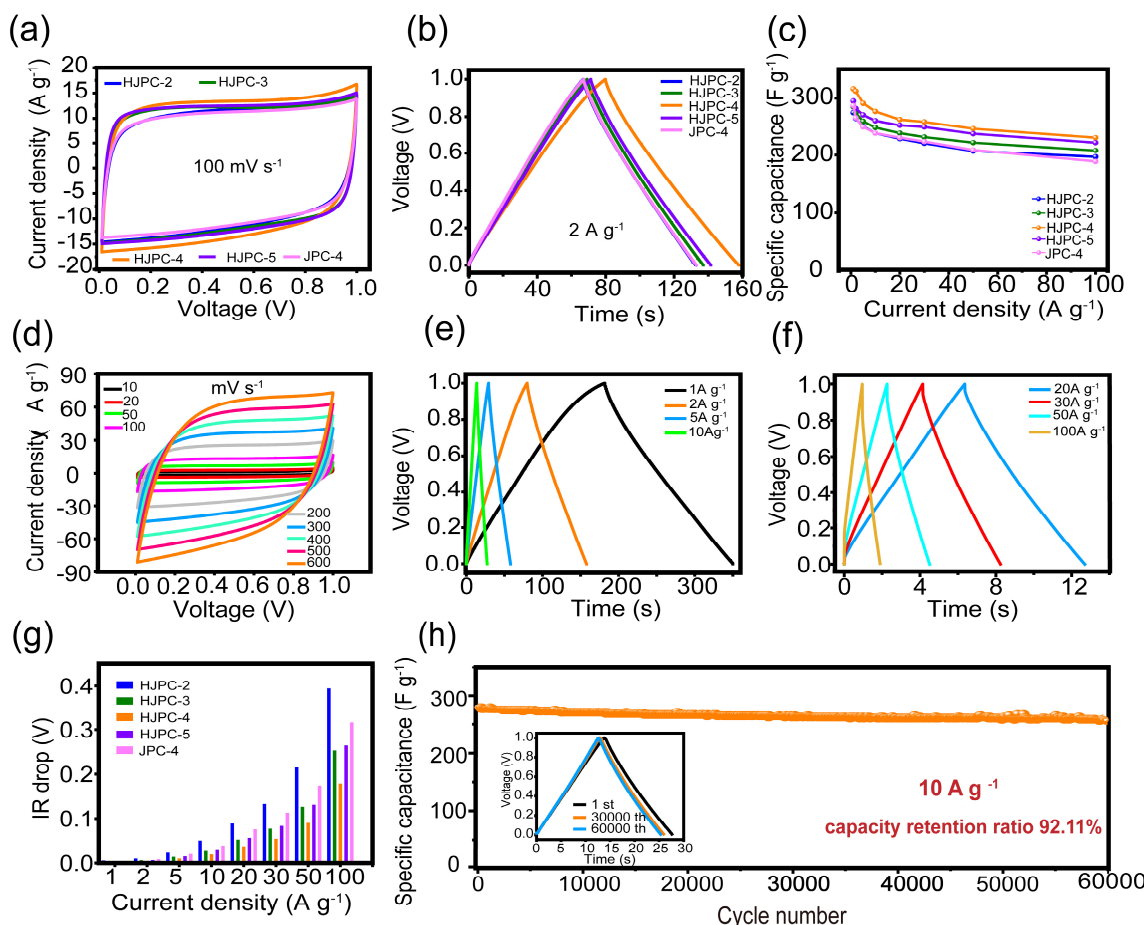


Figure 5. Electrochemical performance of HJPC-X and JPC-4 in the symmetrical supercapacitors using 6 M KOH as electrolyte. (a) CV curves at 100 mV s^{-1} , (b) GCD curves at 2 A g^{-1} , (c) rate capability of HJPC-X and JPC-4. (d) CV curves at different scan rates, (e,f) GCD curves of HJPC-4. (g) IR drop histograms of HJPC-X and JPC-4. (h) Cycling performance at 10 A g^{-1} of HJPC-4.

To distinguish the EDLC of HJPC-X and JPC-4, the specific capacitance was divided into a rate-independent part and a diffusion-limited part based on a widely recognized theory [18]. As observed in Figure S4, the rate-independent part (intercept of the linear portion fitting) of HJPC-X is much higher than that of JPC-4, which reveals the positive effect of hydrothermal treatment on the EDLC capacitance of carbon materials. In addition, the IR drop histograms of HJPC-X and JPC-4 are shown in Figure 5g, where HJPC-4 exhibits the lowest IR drop (only 0.174 V at 100 A g⁻¹). Such a low IR drop is beneficial for the improvement of energy density at fast-charging conditions. As exhibited in Figure 5h, HJPC-4 exhibits excellent cycling stability in 6 M KOH with capacitance retention of 92.11% after 60,000 cycles at 10 A g⁻¹. In addition, the isosceles triangle of the GCD curve remains well preserved after 60,000 cycles, indicating the high reversibility of HJPC-4.

Based on the energy density equation, the operating voltage is the most critical parameter to determine the energy density of supercapacitors [45]. To optimize the energy density of HJPC-X, we selected EMIMBF₄ with a wide operating voltage as the electrolyte to assemble the symmetric supercapacitors. The CV curves of HJPC-X and JPC-4 at 100 mV s⁻¹ are shown in Figure 6a, and all the CV curves of HJPC-X show a quasi-rectangular shape without significant polarization. Correspondingly, the GCD curves at 5 A g⁻¹ exhibit an approximate isosceles triangle shape (Figure 6b). These two facts indicate their EDLC-based energy storage mechanism and their ability to operate stably at a high voltage window of 3.6 V [46]. The rate capability of HJPC-X and JPC-4 is displayed in Figure 6c. As expected, HJPC-4 exhibits a superior specific capacitance to the other samples at all current densities. Specifically, HJPC-4 provides an impressive specific capacitance of 204 F g⁻¹ at 1 A g⁻¹ and maintains 154 F g⁻¹ even at 30 A g⁻¹ with a capacity retention rate of 75.5%. In contrast, JPC-4 without hydrothermal treatment exhibits an unsatisfactory rate performance (46 F g⁻¹ at 30 A g⁻¹). Apparently, the ion-migration blocking effect induced by the absence of pores above 3 nm suppresses the rate performance of JPC-4. Furthermore, the CV curve of HJPC-X maintains a near-rectangular shape even at 300 mV s⁻¹, while JPC-4 deviates from the rectangular shape as the scan rate increases (Figures 6d and S5), further demonstrating the decisive role of supermesopores and macropores on its rate performance [47]. In Figure 6e, the near-isosceles GCD curves of HJPC-4 at different current densities reaffirm the EDLC-dominated energy storage mechanism.

The energy storage kinetics of HJPC-X and JPC-4 were analyzed by electrochemical impedance spectroscopy (EIS). Nyquist plots and a magnified schematic of the high-frequency region are displayed in Figure 6f. In the low-frequency region, HJPC-4 exhibits the maximum slope, which indicates its minimum interface transfer resistance. In the medium-frequency region, the shortest length of the 45° diagonal line of HJPC-4 demonstrates its smallest ion diffusion resistance, which is favorable to the rapid diffusion of active ions from the electrolyte to the electrode. In the high-frequency region, the smallest diameter of the semicircle of HJPC-4 indicates that HJPC-4 has the smallest charge transfer resistance [18]. As shown in Figure 6g, consistent with the EIS results, HJPC-4 has the lowest IR drop with an IR drop of only 0.372 V even at a high current of 30 A g⁻¹. In addition, HJPC-4 exhibits excellent cycling stability in EMIMBF₄, as shown in Figure 6h. It has an initial specific capacitance of up to 185 F g⁻¹ and capacitance retention of 80% after 10,000 cycles at 5 A g⁻¹.

The energy/power density of SCs is an important indicator to assess their practical application capability. Ragone plots of HJPC-4 based on 6 M KOH and EMIMBF₄ electrolyte are displayed in Figure 7a. HJPC-4 with 6 M KOH electrolyte exhibits the maximum energy density of 10.92 Wh kg⁻¹ at a power density of 250 W kg⁻¹ and still holds 5.42 Wh kg⁻¹ at the maximum power density of 20.98 kW kg⁻¹. Moreover, when the electrolyte is changed to EMIMBF₄ with a wide voltage window of 3.6 V, HJPC-4 can provide an ultra-high

energy density of 91.09 Wh kg^{-1} at a power density of 896 W kg^{-1} , and it can still contribute a high energy density of 55.72 Wh kg^{-1} even at the ultimate power density of 24.25 kW kg^{-1} , which is significantly superior to the recently reported biomass-based carbon materials [28,48–57]. As shown in Figure 7b, a fully charged symmetric supercapacitors at 5 A g^{-1} can easily light up a pattern made of dozens of yellow light-emitting diodes soldered together, further demonstrating the great potential of JPs for high-performance supercapacitors. The excellent performance of HJPC-4 can be attributed to two aspects: (1) the large ion-accessible pore volume ($V_{0.5\text{--}3\text{nm}} = 1.025 \text{ cm}^3 \text{ g}^{-1}$, $V_{0.76\text{--}3\text{nm}} = 1.067 \text{ cm}^3 \text{ g}^{-1}$) can provide abundant active sites for charge accumulation; (2) the considerable supermesopore and macropore volume ($V_{d>3\text{nm}} = 0.29 \text{ cm}^3 \text{ g}^{-1}$) can effectively alleviate the ion “plugging effect”, thereby providing fast channels for ion diffusion at the electrode/electrolyte interface and transport inside the electrode.

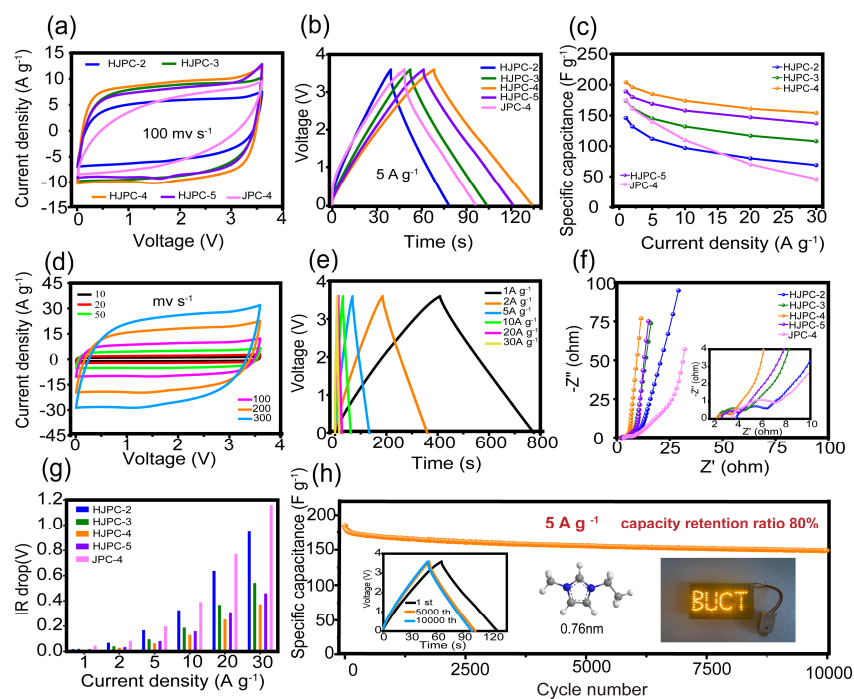


Figure 6. Electrochemical performance of HJPC-X and JPC-4 in the symmetrical supercapacitors using EMIMBF₄ as electrolyte. (a) CV curves at 100 mV s^{-1} , (b) GCD curves at 5 A g^{-1} , (c) rate capability of HJPC-X and JPC-4. (d) CV curves at different scan rates. (e) GCD curves at different current densities of HJPC-4. (f) Nyquist plots (inset is the high frequency section), (g) IR drop histograms of HJPC-X and JPC-4. (h) Cycling stability at 5 A g^{-1} of HJPC-4.

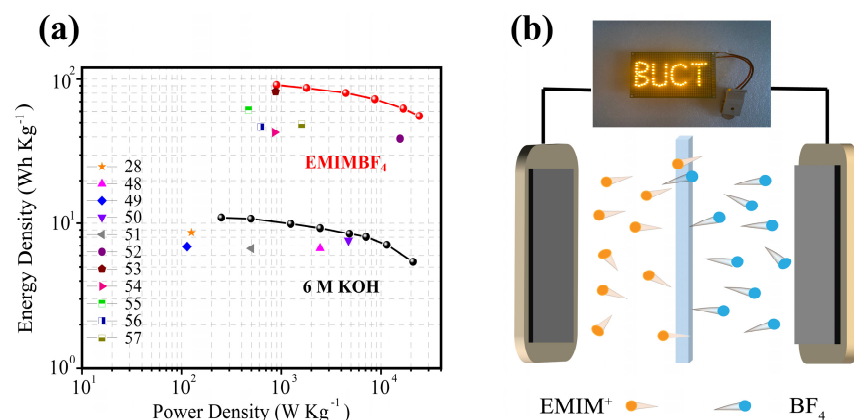


Figure 7. (a) Ragone plots of HJPC-4 in 6 M KOH and EMIMBF₄ and comparison with related works; (b) photograph of LEDs powered by HJPC-4.

4. Conclusions

In summary, using waste jujube pits as the precursor, we have successfully fabricated a hierarchical porous carbon with a rational pore structure through the combination of hydrothermal treatment and subsequent KOH activation. The structural characterization indicates that hydrothermal treatment and KOH activation play crucial roles in modulating the micropores and large-size pores ($d > 3$ nm) contents of the product, respectively. The symmetrical supercapacitors assembled based on the optimized HJPC-4 electrode in a 6 M KOH electrolyte can contribute an ultra-high specific capacity of 316 F g^{-1} at 1 A g^{-1} , a high capacitance retention of 73.1% even at 100 A g^{-1} , and a capacitance loss of only 7.89% after 60,000 cycles at 10 A g^{-1} . In addition, HJPC-4 can operate stably at a high operating voltage of 3.6 V and deliver an extremely high energy/power density of $91.09 \text{ Wh kg}^{-1}/24.25 \text{ kW kg}^{-1}$ in EMIMBF₄ electrolyte. This work presents insights into the effect mechanism of pore structure on the electrochemical performance of carbon-based materials.

Supplementary Materials: The following supporting information can be downloaded at <https://www.mdpi.com/article/10.3390/batteries11010007/s1>, Figure S1: SEM images; Figure S2: XPS spectra; Figure S3, Figure S4 and Figure S5: Electrochemical performance; Table S1: Pore structure parameters; Table S2: Surface element composition.

Author Contributions: Conceptualization, C.K. and D.Q.; Data curation, M.Z. and C.Q.; Formal analysis, C.K., M.Z., C.Q., F.Z., Y.W., Z.C., T.L. and D.Q.; Investigation, C.K. and M.Z.; Methodology, C.K., M.Z. and D.Q.; Project administration, D.Q.; Software, C.K. and C.Q.; Supervision, D.Q.; Validation, C.K. and M.Z.; Writing—original draft, C.K. and M.Z.; Writing—review and editing, D.Q. All authors have read and agreed to the published version of the manuscript.

Funding: This research was funded by the National Natural Science Foundation of China (52402278), the Yichang Natural Science Research Project (A24-3-013), and the Science Foundation of China Three Gorges University (2023RCKJ0021).

Data Availability Statement: Data are contained within the article or Supplementary Materials.

Conflicts of Interest: Author Chang Qiu was employed by the company China Construction Third Engineering Bureau Group Co., Ltd. The remaining authors declare that the research was conducted in the absence of any commercial or financial relationships that could be construed as a potential conflict of interest.

References

1. Liu, X.; Lyu, D.; Merlet, C.; Leesmith, M.J.A.; Hua, X.; Xu, Z.; Grey, C.P.; Forse, A.C. Structural disorder determines capacitance in nanoporous carbons. *Science* **2024**, *384*, 321–325. [[CrossRef](#)] [[PubMed](#)]
2. Fang, L.; Liu, K.; Xu, L.; Wu, F.; Borch, T.; Li, F. Rechargeable carbonaceous geosupercapacitor for sustainable superoxide generation and pollutant abatement. *Nat. Water* **2024**, *2*, 485–495. [[CrossRef](#)]
3. Zubairi, H.; Lu, Z.; Zhu, Y.; Reaney, I.M.; Wang, G. Current development, optimisation strategies and future perspectives for lead-free dielectric ceramics in high field and high energy density capacitors. *Chem. Soc. Rev.* **2024**, *53*, 10761–10790. [[CrossRef](#)] [[PubMed](#)]
4. Yang, W.; Wang, P.; Tu, Z.; Hou, L.; Yan, L.; Jiang, B.; Zhang, C.; Huang, G.; Yang, F.; Li, Y. Heteroatoms-doped hierarchical porous carbon with multi-scale structure derived from petroleum asphalt for high-performance supercapacitors. *Carbon* **2022**, *187*, 338–348. [[CrossRef](#)]
5. Yang, J.; Wu, H.; Zhu, M.; Ren, W.; Lin, Y.; Chen, H.; Pan, F. Optimized mesopores enabling enhanced rate performance in novel ultrahigh surface area meso-/microporous carbon for supercapacitors. *Nano Energy* **2017**, *33*, 453–461. [[CrossRef](#)]
6. Qiu, D.; Wang, Y.; Zhang, L.; Lei, H.; Ying, H.; Niu, J.; Li, M.; Yang, X.; Wang, F.; Yang, R. Regulating the oxygen-atom configuration of carbon anode enabling extremely fast-charging potassium-ion hybrid capacitors. *Nano Res.* **2025**, *18*, 94907033. [[CrossRef](#)]
7. Wang, J.; Zheng, F.; Yu, Y.; Hu, P.; Li, M.; Wang, J.; Fu, J.; Zhen, Q.; Bashir, S.; Liu, J.L. Symmetric supercapacitors composed of ternary metal oxides (NiO/V₂O₅/MnO₂) nanoribbon electrodes with high energy storage performance. *Chem. Eng. J.* **2021**, *426*, 131804. [[CrossRef](#)]

8. Fong, K.D.; Wang, T.; Kim, H.K.; Kumar, R.V.; Smoukov, S.K. Semi-Interpenetrating Polymer Networks for Enhanced Supercapacitor Electrodes. *ACS Energy Lett.* **2017**, *2*, 2014–2020. [[CrossRef](#)] [[PubMed](#)]
9. Chen, Z.; Ye, S.; Evans, S.D.; Ge, Y.; Zhu, Z.; Tu, Y.; Yang, X. Confined Assembly of Hollow Carbon Spheres in Carbonaceous Nanotube: A Spheres-in-Tube Carbon Nanostructure with Hierarchical Porosity for High-Performance Supercapacitor. *Small* **2018**, *14*, 1704015. [[CrossRef](#)]
10. Chen, S.; Wang, W.; Zhang, X.; Wang, X. High-Performance Supercapacitors Based on Graphene/Activated Carbon Hybrid Electrodes Prepared via Dry Processing. *Batteries* **2024**, *10*, 195. [[CrossRef](#)]
11. Yan, Z.; Gao, Z.; Zhang, Z.; Dai, C.; Wei, W.; Shen, P.K. Graphene Nanosphere as Advanced Electrode Material to Promote High Performance Symmetrical Supercapacitor. *Small* **2021**, *17*, 2007915. [[CrossRef](#)] [[PubMed](#)]
12. Wang, L.; Liu, R. Knitting Controllable Oxygen-Functionalized Carbon Fiber for Ultrahigh Capacitance Wire-Shaped Supercapacitors. *ACS Appl. Mater. Interfaces* **2020**, *12*, 44866–44873. [[CrossRef](#)]
13. Song, M.; Zhou, Y.; Ren, X.; Wan, J.; Du, Y.; Wu, G.; Ma, F. Biowaste-based porous carbon for supercapacitor: The influence of preparation processes on structure and performance. *J. Colloid Interface Sci.* **2019**, *535*, 276–286. [[CrossRef](#)] [[PubMed](#)]
14. Yue, T.; Shen, B.; Gao, P. Carbon material/MnO₂ as conductive skeleton for supercapacitor electrode material: A review. *Renew. Sustain. Energy Rev.* **2022**, *158*, 112131. [[CrossRef](#)]
15. Lu, W.; Si, Y.; Zhao, C.; Chen, T.; Li, C.; Zhang, C.; Wang, K. Biomass-derived carbon applications in the field of supercapacitors: Progress and prospects. *Chem. Eng. J.* **2024**, *495*, 153311. [[CrossRef](#)]
16. Szczęśniak, B.; Phuriragpitikhon, J.; Choma, J.; Jaroniec, M. Recent advances in the development and applications of biomass-derived carbons with uniform porosity. *J. Mater. Chem. A* **2020**, *8*, 18464–18491. [[CrossRef](#)]
17. Luo, L.; Lan, Y.; Zhang, Q.; Deng, J.; Luo, L.; Zeng, Q.; Gao, H.; Zhao, W. A review on biomass-derived activated carbon as electrode materials for energy storage supercapacitors. *J. Energy Storage* **2022**, *55*, 105839. [[CrossRef](#)]
18. Qiu, D.; Li, M.; Kang, C.; Wei, J.; Wang, F.; Yang, R. Cucurbit[6]uril-Derived Sub-4 nm Pores-Dominated Hierarchical Porous Carbon for Supercapacitors: Operating Voltage Expansion and Pore Size Matching. *Small* **2020**, *16*, 2002718. [[CrossRef](#)]
19. Li, D.; Huang, Y.; Yu, C.; Lu, Y.; Tang, C.; Lin, J. Pore structure regulation of hierarchical porous agaric-derived carbon via boric acid activation for supercapacitors. *Diam. Relat. Mater.* **2022**, *130*, 109432. [[CrossRef](#)]
20. Chen, S.; Fang, S.; Lim, A.I.; Bao, J.; Hu, Y.H. 3D meso/macroporous carbon from MgO-templated pyrolysis of waste plastic as an efficient electrode for supercapacitors. *Chemosphere* **2023**, *322*, 138174. [[CrossRef](#)] [[PubMed](#)]
21. Shah, S.S. Biomass-Derived Carbon Materials for Advanced Metal-Ion Hybrid Supercapacitors: A Step Towards More Sustainable Energy. *Batteries* **2024**, *10*, 168. [[CrossRef](#)]
22. Zhang, M.; Jiang, S.; Zou, J.; Qu, X.; Zhang, Z.; Wang, R.; Qiu, S. N-Doped Yolk–Shell Carbon Nanospheres with “Carbon Bridges” for Supercapacitors. *ACS Appl. Nano Mater.* **2023**, *6*, 8279–8289. [[CrossRef](#)]
23. Guo, N.; Li, M.; Sun, X.; Wang, F.; Yang, R. Enzymatic hydrolysis lignin derived hierarchical porous carbon for supercapacitors in ionic liquids with high power and energy densities. *Green Chem.* **2017**, *19*, 2595–2602. [[CrossRef](#)]
24. Liu, C.; Han, M.; Lin, J.; Liu, W.; Liu, J.; Zeng, Z. Wood biomass-derived carbon for high-performance electromagnetic wave absorbing and shielding. *Carbon* **2023**, *208*, 255–276. [[CrossRef](#)]
25. Wang, L.; Ma, X.; Ma, Z.; Li, P.; Zhang, L. KHCO₃ Chemical-Activated Hydrothermal Porous Carbon Derived from Sugarcane bagasse for Supercapacitor Applications. *Chem Asian J.* **2024**, *19*, e202400530. [[CrossRef](#)] [[PubMed](#)]
26. Mohit, Y.N.; Hashmi, S.A. High energy density solid-state supercapacitors based on porous carbon electrodes derived from pre-treated bio-waste precursor sugarcane bagasse. *J. Energy Storage* **2022**, *55*, 105421. [[CrossRef](#)]
27. Liu, R.; Wang, J.-X.; Yang, W.-D. Hierarchical Porous Heteroatoms—Co-Doped Activated Carbon Synthesized from Coconut Shell and Its Application for Supercapacitors. *Nanomaterials* **2022**, *12*, 3504. [[CrossRef](#)]
28. He, C.; Huang, M.; Zhao, L.; Lei, Y.; He, J.; Tian, D.; Zeng, Y.; Shen, F.; Zou, J. Enhanced electrochemical performance of porous carbon from wheat straw as remolded by hydrothermal processing. *Sci. Total Environ.* **2022**, *842*, 156905. [[CrossRef](#)] [[PubMed](#)]
29. Gong, Y.; Li, D.; Fu, Q.; Zhang, Y.; Pan, C. Nitrogen Self-Doped Porous Carbon for High-Performance Supercapacitors. *ACS Appl. Energy Mater.* **2020**, *3*, 1585–1592. [[CrossRef](#)]
30. Yuan, M.; Wang, Z.; Rao, Y.; Wang, Y.; Gao, B.; Yu, J.; Li, H.; Chen, X. Laser direct writing O/N/S Co-doped hierarchically porous graphene on carboxymethyl chitosan/lignin-reinforced wood for boosted microsupercapacitor. *Carbon* **2023**, *202*, 296–304. [[CrossRef](#)]
31. Pallavolu, M.R.; Prabhu, S.; Nallapureddy, R.R.; Kumar, A.S.; Banerjee, A.N.; Joo, S.W. Bio-derived graphitic carbon quantum dot encapsulated S- and N-doped graphene sheets with unusual battery-type behavior for high-performance supercapacitor. *Carbon* **2023**, *202*, 93–102. [[CrossRef](#)]
32. Guo, T.; Zhou, D.; Pang, L.; Sun, S.; Zhou, T.; Su, J. Perspectives on Working Voltage of Aqueous Supercapacitors. *Small* **2022**, *18*, 2106360. [[CrossRef](#)]
33. Yeletsky, P.M.; Lebedeva, M.V.; Yakovlev, V.A. Today’s progress in the synthesis of porous carbons from biomass and their application for organic electrolyte and ionic liquid based supercapacitors. *J. Energy Storage* **2022**, *50*, 104225. [[CrossRef](#)]

34. Jiang, X.; Wu, X.; Xie, Y.; Wang, Z.; Huang, J.; Qu, Y.; Mu, D.; Zhang, X.; Yang, W.; Zhang, H. Additive Engineering Enables Ionic-Liquid Electrolyte-Based Supercapacitors to Deliver Simultaneously High Energy and Power Density. *ACS Sustain. Chem. Eng.* **2023**, *11*, 5685–5695. [[CrossRef](#)]
35. Nouri, M. Potentials and challenges of date pits as alternative environmental clean-up ingredients. *Biomass Conv. Bioref.* **2023**, *13*, 1429–1456. [[CrossRef](#)]
36. Liu, H.; Wang, Y.; Lv, L.; Liu, X.; Wang, Z.; Liu, J. Oxygen-enriched hierarchical porous carbons derived from lignite for high-performance supercapacitors. *Energy* **2023**, *269*, 126707. [[CrossRef](#)]
37. Xue, B.; Xu, J.; Xiao, R. Ice template-assisting activation strategy to prepare biomass-derived porous carbon cages for high-performance Zn-ion hybrid supercapacitors. *Chem. Eng. J.* **2023**, *454*, 140192. [[CrossRef](#)]
38. Wang, M.-x.; He, D.; Zhu, M.; Wu, L.; Wang, Z.; Huang, Z.-H.; Yang, H. Green fabrication of hierarchically porous carbon micro-tubes from biomass waste via self-activation for high-energy-density supercapacitor. *J. Power Sources* **2023**, *560*, 232703. [[CrossRef](#)]
39. Yang, Z.-H.; Cao, J.-P.; Zhuang, Q.-Q.; Wu, Y.; Zhou, Z.; Wei, Y.-L.; Zhao, X.-Y. Oxygen-enriched porous carbon derived from acid washed and oxidized lignite via H_3PO_4 hydrothermal for high-performance supercapacitors. *Fuel Process. Technol.* **2023**, *243*, 107665. [[CrossRef](#)]
40. Qin, Y.; Miao, L.; Mansuer, M.; Hu, C.; Lv, Y.; Gan, L.; Liu, M. Spatial Confinement Strategy for Micelle-Size-Mediated Modulation of Mesopores in Hierarchical Porous Carbon Nanosheets with an Efficient Capacitive Response. *ACS Appl. Mater. Interfaces* **2022**, *14*, 33328–33339. [[CrossRef](#)] [[PubMed](#)]
41. Qiu, C.; Zuo, M.; Qiu, D.; Cao, J.; Jia, X.; Li, Y.; Liu, C.; Chen, N.; Chen, X.; Li, M. Unique hierarchical porous carbon nanosheet network for supercapacitors: Ultra-long cycling stability and enhanced electroactivity of oxygen at high temperature. *Electrochim. Acta* **2023**, *437*, 141522. [[CrossRef](#)]
42. Eftekhari, A. Supercapacitors utilising ionic liquids. *Energy Storage Mater.* **2017**, *9*, 47–69. [[CrossRef](#)]
43. Abdelaal, M.M.; Hung, T.-C.; Mohamed, S.G.; Yang, C.-C.; Hung, T.-F. Two Birds with One Stone: Hydrogel-Derived Hierarchical Porous Activated Carbon toward the Capacitive Performance for Symmetric Supercapacitors and Lithium-Ion Capacitors. *ACS Sustain. Chem. Eng.* **2022**, *10*, 4717–4727. [[CrossRef](#)]
44. Chen, B.; Wu, D.; Wang, T.; Yuan, F.; Jia, D. Rapid preparation of porous carbon by flame burning carbonization method for supercapacitor. *Chem. Eng. J.* **2023**, *462*, 142163. [[CrossRef](#)]
45. Sun, L.; Zhuo, K.; Chen, Y.; Du, Q.; Zhang, S.; Wang, J. Ionic Liquid-Based Redox Active Electrolytes for Supercapacitors. *Adv. Funct. Mater.* **2022**, *32*, 2203611. [[CrossRef](#)]
46. Nguyen, T.B.; Yoon, B.; Nguyen, T.D.; Oh, E.; Ma, Y.; Wang, M.; Suhr, J. A facile salt-templating synthesis route of bamboo-derived hierarchical porous carbon for supercapacitor applications. *Carbon* **2023**, *206*, 383–391. [[CrossRef](#)]
47. Liu, Q.; Wu, D.; Wang, T.; Guo, Y. Polysaccharide of agar based ultra-high specific surface area porous carbon for superior supercapacitor. *Int. J. Biol. Macromol.* **2023**, *228*, 40–47. [[CrossRef](#)]
48. Wan, X.; Shen, F.; Hu, J.; Huang, M.; Zhao, L.; Zeng, Y.; Tian, D.; Yang, G.; Zhang, Y. 3-D hierarchical porous carbon from oxidized lignin by one-step activation for high-performance supercapacitor. *Int. J. Biol. Macromol.* **2021**, *180*, 51–60. [[CrossRef](#)] [[PubMed](#)]
49. Selvaraj, A.R.; Chinnadurai, D.; Cho, I.; Bak, J.-S.; Prabakar, K. Bio-waste wood-derived porous activated carbon with tuned microporosity for high performance supercapacitors. *J. Energy Storage* **2022**, *52*, 104928. [[CrossRef](#)]
50. Liu, Z.; Hu, J.; Shen, F.; Tian, D.; Huang, M.; He, J.; Zou, J.; Zhao, L.; Zeng, Y. Trichoderma bridges waste biomass and ultra-high specific surface area carbon to achieve a high-performance supercapacitor. *J. Power Sources* **2021**, *497*, 229880. [[CrossRef](#)]
51. Dhakal, G.; Mohapatra, D.; Kim, Y.-I.; Lee, J.; Kim, W.K.; Shim, J.-J. High-performance supercapacitors fabricated with activated carbon derived from lotus calyx biowaste. *Renew. Energy* **2022**, *189*, 587–600. [[CrossRef](#)]
52. Qin, C.; Wang, S.; Wang, Z.; Ji, K.; Wang, S.; Zeng, X.; Jiang, X.; Liu, G. Hierarchical porous carbon derived from *Gardenia jasminoides* Ellis flowers for high performance supercapacitor. *J. Energy Storage* **2021**, *33*, 102061. [[CrossRef](#)]
53. Wu, Y.; Cao, J.-P.; Zhuang, Q.-Q.; Zhao, X.-Y.; Zhou, Z.; Wei, Y.-L.; Zhao, M.; Bai, H.-C. Biomass-derived three-dimensional hierarchical porous carbon network for symmetric supercapacitors with ultra-high energy density in ionic liquid electrolyte. *Electrochim. Acta* **2021**, *371*, 137825. [[CrossRef](#)]
54. Wang, D.; Xu, L.; Nai, J.; Bai, X.; Sun, T. Morphology-controllable synthesis of nanocarbons and their application in advanced symmetric supercapacitor in ionic liquid electrolyte. *Appl. Surf. Sci.* **2019**, *473*, 1014–1023. [[CrossRef](#)]
55. Guo, N.; Luo, W.; Guo, R.; Qiu, D.; Zhao, Z.; Wang, L.; Jia, D.; Guo, J. Interconnected and hierarchical porous carbon derived from soybean root for ultrahigh rate supercapacitors. *J. Alloys Compd.* **2020**, *834*, 155115. [[CrossRef](#)]

56. Ding, Y.; Qi, J.; Hou, R.; Liu, B.; Yao, S.; Lang, J.; Chen, J.; Yang, B. Preparation of High-Performance Hierarchical Porous Activated Carbon via a Multistep Physical Activation Method for Supercapacitors. *Energy Fuels* **2022**, *36*, 5456–5464. [[CrossRef](#)]
57. Li, Y.; Zhang, D.; Zhang, Y.; He, J.; Wang, Y.; Wang, K.; Xu, Y.; Li, H.; Wang, Y. Biomass-derived microporous carbon with large micropore size for high-performance supercapacitors. *J. Power Sources* **2020**, *448*, 227396. [[CrossRef](#)]

Disclaimer/Publisher’s Note: The statements, opinions and data contained in all publications are solely those of the individual author(s) and contributor(s) and not of MDPI and/or the editor(s). MDPI and/or the editor(s) disclaim responsibility for any injury to people or property resulting from any ideas, methods, instructions or products referred to in the content.